

1 **Spectral characteristics of turbulent**
2 **wind-driven gyre flow**

3 F.J. Poulin *

Department of Applied Mathematics,
University of Waterloo,
Waterloo, ON, Canada, N2L 3G1

B. Fox-Kemper

Department of Atmospheric and Oceanic Sciences,
University of Colorado at Boulder,
Boulder, CO, 80309-0216, USA,

N. K.-R. Kevlahan

Department of Mathematics and Statistics,
McMaster University,
Hamilton, ON, L8S 4K1, Canada,

W. Ko

Department of Mathematics,,
Simon Fraser University,
Burnaby, BC, V5A 1S6, Canada,

4 February 11, 2012

6 We compare quasi-geostrophic (QG) simulations of a wind-driven gyre to a barotropic rotat-
 7 ing shallow water (SW) model with a free-surface, focusing on energy spectra and spectral
 8 transfers at statistical forced-dissipative equilibrium. In the turbulent regime these two
 9 models generally agree. The SW simulations are computationally expensive, but also more
 10 accurate because they resolve some aspects of three dynamically distinct regimes: synoptic
 11 scales, mesoscales and the barotropic submesoscales. In contrast, QG is only valid in the
 12 mesoscale. Although the submesoscale is not fully resolved, ageostrophic flow is detected. In
 13 both the turbulent SW and QG simulations there is a critical scale between the Munk layer
 14 thickness (the width of positive shear layer next to the wall) and the inertial boundary layer
 15 thickness (the width of the jet) that fixes the size of the eddies generated by the barotropic
 16 instability of the Western Boundary Current. These eddies inject energy into the basin and
 17 this critical scale is therefore analogous to the intermediate forcing scale used in simulations
 18 of two-dimensional turbulence. We find that, similar to forced two-dimensional turbulence,
 19 the energy spectrum of the flow in the mesoscale regime above this critical scale follows a
 20 power-law of $-5/3$ due to an inverse energy cascade, while below this scale the power-law
 21 is -5 . The perturbation energy spectrum has a power law closer to -3 at scales smaller
 22 than the forcing scale, which is consistent with freely evolving two-dimensional turbulence.
 23 Furthermore, we use the Wavelet transform to compute the localized spectra in a turbulent
 24 subdomain away from the WBC and find three dynamical ranges in the flow.

25 1. Introduction

26 Ocean dynamics are still poorly understood, in part because they extend over a vast
 27 range of length scales, from planetary to sub-millimetre. Many forces that drive the oceans,
 28 such as winds, gravity and solar heating, introduce energy on planetary length scales that

*Corresponding author address: Francis Poulin, E-mail: fpoulin@uwaterloo.ca

29 is transferred down to smaller and smaller length scales by turbulence before it is finally
30 dissipated to heat via molecular viscosity. Indeed, it is because turbulence is an essential
31 component of ocean dynamics that predicting the evolution of the oceans at all length scales
32 seems to be an impossible task, but it is what is required—at least in approximation—to
33 understand the oceans at any scale.

34 From data it is obvious that the dominant features of the large-scale oceanographic
35 circulation are sub-tropical and sub-polar gyre circulation that dominate the extratropical
36 circulation. Sverdrup (1947) showed that meridional variation in the atmospheric winds
37 drives the slow gyre circulations in the majority of the ocean basins. Associated with each
38 gyre is a highly energetic, relatively narrow, Western Boundary Current (WBC) that nearly
39 balances the meridional transport of the Sverdrup gyre circulation. Shortly thereafter, Stom-
40 mel (1948) and Munk (1950) both explained that the preference for western intensification
41 in the oceans is because the vorticity added by the winds can only be dissipated along the
42 western boundary. The beauty of these simple theories is that their predictions agree quali-
43 tatively with what is observed in the world’s oceans on the planetary, or gyre, scales. Their
44 major shortcoming is that the necessary dissipation is provided by parameterizing unresolved
45 smaller scale (turbulent) motions. This is because these models describe only the largest
46 scales, and as a result they necessarily obtain laminar flow. This is in contrast with our
47 observations that the oceans are strongly turbulent.

48 To understand the real ocean it is necessary to include turbulence, and this requires
49 resolving a much wider range of length scales. State of the art atmosphere-ocean general
50 circulation Models (AOGCMs) are eddy permitting in that they are able to resolve some
51 aspects of mesoscale eddies (McClean et al. 2011). In order to quantify the effect of the
52 smaller length scales, such as the submesoscale, on the resolved motions it is necessary to
53 parameterize (Fox-Kemper et al. 2008; Fox-Kemper and Ferrari 2008; Fox-Kemper et al.
54 2011) or investigate idealized models (Lévy et al. 2010), which is the approach we take here.
55 The particular idealized model we use is a barotropic, Shallow Water (SW) ocean with a

56 free surface in the confines of a square ocean basin with solid walls on each boundary. The
57 simplicity of this model prevents us from addressing many aspects of ocean circulation, but
58 it does allow us to analyze the barotropic dynamics of a wind-driven ocean in finer detail
59 than has been done previously.

60 In the oceanographic community it is usually agreed that the gyre scale, mesoscale and
61 submesoscale are roughly $O(1\,000\text{ km})$, $O(100\text{ km})$ and $O(10\text{ km})$, respectively. The second
62 largest scale, the mesoscale, is characterized by the interaction of eddies (or coherent vor-
63 tices) that are inherently nonlinear oceanographic features. They can persist for several
64 months and propagate over great distances (Carton 2000). In our context it is useful to
65 associate the mesoscale with the dynamical regime that includes both the external radius
66 of deformation and the inertial boundary layer thickness (Charney 1955) (to be defined ex-
67 plicitly in the following section). By this choice, we define the (barotropic) mesoscale to
68 be the regime where the relative vorticity gradient is similar in magnitude to the planetary
69 vorticity gradient ($\nabla \times u_h \sim \beta y \ll f_0$).¹ QG dynamics are asymptotically appropriate for
70 this definition of the mesoscale (Grooms et al. 2011).

71 The submesoscale is more difficult to define. Recently, Capet et al. (2008a) define subme-
72 soscale motions as motions with horizontal length scales of $O(10\text{ km})$, but also having three
73 essential characteristics: 1) they are generated from mesoscale currents and thus are distinct
74 from from inertia-gravity waves, 2) they are strongly influenced by rotation and 3) they are
75 surprisingly energetic in comparison to QG turbulence. An alternative definition put forward
76 by Thomas et al. (2008) is that submesoscale motions are those defined by order one Rossby
77 numbers and they are necessarily ageostrophic (i.e. the Coriolis force and pressure gradient
78 are no longer in balance). Since the submesoscale is usually considered to be the length
79 scales at which the QG approximation breaks down, we will use the latter definition in the
80 barotropic context. Thus, we consider the submesoscale to be the scale where the relative

¹Note that this does not imply that the relative vorticity is as large as the planetary, as the scale of variation of the latter is much larger.

81 vorticity is similar in magnitude to the planetary vorticity ($\beta y \ll \nabla \times u_h \sim f_0$). We propose
82 that this be called the *barotropic submesoscale* to differentiate it from the more common
83 version that is used in the context of a stratified ocean. Thomas et al. (2008) points out
84 that submesoscale features tend to differ from inertia-gravity waves in that they are more
85 balanced but also that submesoscale motions are inherently generated from mechanisms that
86 modify Potential Vorticity (PV), such as wind forcing, buoyancy flux and friction. Another
87 definition of submesoscale is order one Burger number based on the deformation radius of
88 the mixed layer (Boccaletti et al. 2007; Hosegood et al. 2006), but this definition will not be
89 appropriate in our barotropic context.

90 In this paper we present results from a variety of numerical simulations of wind-driven
91 gyre flow in the context of both one-layer SW and QG models to elucidate the nature of
92 the barotropic dynamics. These numerical experiments use high-accuracy pseudo-spectral
93 numerical methods that we have developed to resolve the widest possible range of length
94 and time scales for a given number of grid points. In particular, we resolve the gyre scale,
95 mesoscale and a limited part of the barotropic submesoscale. Comparisons are done with
96 a rigid-lid, barotropic QG model that we also developed and which uses similar numerical
97 techniques.

98 The central question that we address is how the energy is transferred across the different
99 length scales due to nonlinear interactions. It is well known that forced two-dimensional
100 turbulence, whose governing equations are similar to the barotropic QG model, has a strong
101 inverse energy cascade (characterized by a $k^{-5/3}$ energy spectrum) and a forward enstro-
102 phy cascade (characterized by a energy spectrum steeper than k^{-3}), consistent with the
103 Batchelor-Leith-Kraichnan theory for homogeneous two-dimensional turbulence (Kraichnan
104 and Montgomery 1980). However, energy in the oceans is eventually transferred to the small
105 three-dimensional length scales and thus there must also be a direct cascade of energy. Con-
106 sequently, there is great interest in understanding the mechanisms that can generate the
107 direct energy cascade to smaller scales (McWilliams 2003; Molemaker et al. 2009). One diffi-

108 culty is that much of our understanding of QG turbulence comes from numerical simulations
109 in periodic domains. In our research we include large-scale forcing by the winds, localized
110 lateral small-scale friction that is scale selective, relatively weak bottom drag and purely
111 barotropic dynamics. Large-scale winds generate and maintain a strong and narrow WBC
112 that is barotropically unstable and radiates eddies into the interior of the gyre. This is to
113 be contrasted with Scott and Arbic (2007) who investigated a forced-dissipative system that
114 had relatively small-scale instabilities (on the order of the internal radius of deformation)
115 and included only bottom drag to damp the inverse energy cascade.

116 Recently, numerous papers have studied forced, two-dimensional turbulence in a closed
117 domain to better understand the effect of the boundaries (van Heijst et al. 2006; van Heijst
118 and Clercx 2009; Clercx and van Heijst 2009). (The freely decaying analogue has been
119 been addressed in Schneider and Farge (2008) for a variety of different geometries.) These
120 investigations are motivated by the need to better understand the turbulence that arises in
121 the oceans and they do help in building our physical understanding of the basic mechanisms.
122 However, the forcing that is typically used is very different from the winds that actually force
123 the ocean's surface. Recently, Nadiga and Straub (2010) have begun to bridge this gap by
124 looking at the turbulence that arises in a QG double gyre due to idealized winds, both steady
125 and stochastic. They found evidence for both a strong inverse energy cascade in the form
126 of vortex mergers (Kevlahan and Farge 1997), as is observed in the classical forced problem,
127 but they also found a direct energy cascade. Our work can be seen as a natural extension of
128 Nadiga and Straub (2010), but for a single gyre in a SW model to allow for non-QG effects.
129 Of primary interest is whether the non-QG effects accentuate or impede the forward energy
130 cascade, as suggested in a different context by Capet et al. (2008b).

131 The outline of the paper is as follows. First, we describe the model that we use and our
132 particular choice of nonlinear viscosity that is consistent with the energetics of the system.
133 Secondly, we present results from the numerical simulations. We emphasize the energy
134 spectra and the spectral transfers (and fluxes), calculated using wavelet analysis. Finally,

135 we conclude our findings and discuss future research directions.

136 2. Barotropic Model of Large-Scale Wind Driven Flow

137 a. Conservative Equations

138 The SW equations are well-known and are derived in most textbooks on geophysical
139 fluid dynamics (Pedlosky 1987a; Vallis 2006; Kundu and Cohen 2008). These equations are
140 limited because they describe the two-dimensional dynamics of a homogeneous fluid, but
141 they are rich in that they include a wide range of horizontal length scales, from gyre to the
142 barotropic submesoscale.

The primitive variables for the SW equations are the horizontal velocity $\mathbf{u}(x, y, t)$ and the total layer depth $h(x, y, t)$. If we assume that the bottom topography and the free-surface are located at $z = h_B(x, y)$ and $z = H + \eta(x, y, t)$, respectively, where H is the mean depth, the governing equations are

$$\frac{D\mathbf{u}}{Dt} + f\mathbf{k} \times \mathbf{u} + g\nabla\eta = \frac{1}{h} [\mathbf{F}_\nu + \tau], \quad (1)$$

$$\frac{Dh}{Dt} + h\nabla \cdot \mathbf{u} = F_h. \quad (2)$$

143 $f = f_0 + \beta y$ is the Coriolis parameter which is a linear approximation assuming a β -plane, g is
144 the acceleration due to gravity (but can also be interpreted as a reduced gravity) and D/Dt
145 is the material (or total) derivative. The right-hand side of these equations includes the non-
146 conservative forces: \mathbf{F}_ν are the viscous forces, τ is the wind-stress due to the atmosphere and
147 F_h are the diabatic forces and unresolved thickness mixing (not considered in this work).
148 Throughout we will assume a flat bottom and allow for a free-surface. The free surface
149 assumption imposes very small time steps due to the need to resolve fast gravity waves and
150 makes these calculations computationally expensive. In contrast, the QG model completely
151 filters out the gravity waves and thus can be integrated numerically using a much larger time
152 step (typically by a factor of 1 000 given the same grid spacing). The model that we use is

153 the same as derived in Pedlosky (1987a).

154 *b. Lateral Eddy Viscosity*

155 In studying geophysical fluids we are faced with the challenge that we are able to resolve
156 only a relatively small range of motions compared to what exists in nature. It is for this rea-
157 son that parameterizations are essential to try to model the influence of the unresolved small
158 length scales on the resolved scales. These subgrid scale parameterizations have many differ-
159 ent forms, but the two most popular are Rayleigh drag (to simulate the effect of bottom drag
160 due due to the Ekman layer) and Laplacian friction (to include lateral viscosity at the walls
161 of the domain). The first two theoretical studies of wind-driven gyre flow are due to Stommel
162 (1948), who included bottom drag, and Munk (1950) who considered lateral viscosity. Both
163 these parameterizations produced the observed western intensification (a northward return
164 flow). Other models have since produced similar results using hyperviscosity (Holland 1978)
165 and spatially variable lateral viscosity (Fox-Kemper and Pedlosky 2004; Fox-Kemper 2004,
166 2005).

One source of friction that is always present in the ocean is molecular viscosity. However, because it only affects the smallest length scales (sub-millimetre) it cannot be included as the sole frictional mechanism in large-scale ocean models, even using the most powerful supercomputers. Because of this, we must resort to other models of viscosity. We choose to include lateral eddy viscosity because it is simple and enables us to enforce no-slip (or slip) boundary conditions in addition to no-normal flow. Lateral viscosity is often included in the SW equations by adding a term proportional to the Laplacian of the velocity to the momentum equations. Unfortunately, as attractive as this choice is, adding this type of friction can actually *increase* kinetic energy (KE), counter to physical intuition. Gent (1993) suggested a slightly different form that does ensure that KE always decreases because

of friction,

$$\mathbf{F}_\nu^g = \frac{\nu}{h} \vec{\nabla} \cdot (h \vec{\nabla} \vec{u}). \quad (3)$$

A slightly more complicated form of eddy viscosity is proposed by Schar and Smith (1993) that is derived by assuming that the dynamic viscosity can be decomposed as $\mu = h\nu$. They then prove that this functional form of friction cannot increase kinetic energy and that the associated stress tensor is symmetric. It has the form in Cartesian components

$$F_\nu^x = \nu \left[\nabla^2 u + (u_x - v_y) \frac{h_x}{h} + (u_y + v_x) \frac{h_y}{h} \right], \quad (4)$$

$$F_\nu^y = \nu \left[\nabla^2 v + (u_y + v_x) \frac{h_x}{h} - (u_x - v_y) \frac{h_y}{h} \right]. \quad (5)$$

167 Schar and Smith (1993) show how it can be obtained by choosing the stress tensor appro-
 168 priately. In the next subsection we show that this is the unique choice that follows from
 169 reducing the viscous term in the three-dimensional equations of motion to the hydrostatic,
 170 two-dimensional limit.

171 *c. Derivation of viscosity for the SW model*

The deviatoric stress tensor for an incompressible Newtonian fluid is

$$\tau_{ij} = \mu \left(\frac{\partial u_i}{\partial x_j} + \frac{\partial u_j}{\partial x_i} \right). \quad (6)$$

172 In the compressible case there is an additional term, but since water is essentially incompress-
 173 ible in three-dimensions this term is neglected. In three dimensions this term is symmetric,
 174 ensuring that angular momentum is conserved (Kundu and Cohen 2008).

In making the shallow water approximation we assume that the motion consists of fluid columns that can be stretched or compressed in the vertical. This requires that the horizontal velocity is independent of depth and we assume the vertical momentum equation reduces to hydrostatic balance. Furthermore, the incompressibility condition means that the vertical divergence must be equal to minus the horizontal divergence. Therefore, in the

above equation even though the horizontal velocity is independent of depth we still include the effects of compressibility in the horizontal. Indeed, by expanding the above equation we find that the modified stress tensor is

$$\tau_{ij} = \mu \left(\frac{\partial u_i}{\partial x_j} + \frac{\partial u_j}{\partial x_i} \right) - \mu \left(\vec{\nabla} \cdot \vec{u} \right) \delta_{ij}, \quad (7)$$

175 where the indices now range only from 1 to 2. Because this form is symmetric in the
 176 horizontal it ensures that angular momentum is conserved in two dimensions, which is no
 177 longer true in three dimensions. The form proposed by Gent (1993) is a reduced form of this
 178 equation that includes the effects of variable viscosity, but neglects entirely the stretching
 179 term (the second term above). This stress tensor is very similar to the deviatoric stress
 180 tensor for compressible flow, but the two coefficients of viscosity are necessarily the same
 181 since they arise from the same source, namely the horizontal viscosity.

The only freedom that we have left is to pick the dynamic viscosity. Inspired by what is done for three-dimensional compressible flows ($\mu = \nu\rho$), we define the kinematic viscosity as $\mu = \nu h$, where we include the effect of spatial variations in the depth field. Therefore, if we compute the divergence of this stress tensor we find that the two viscous momentum equations are, assuming a flat bottom,

$$\frac{Du}{Dt} - fv + g\frac{\partial h}{\partial x} = \nu \left[\nabla^2 u + (u_x - v_y)\frac{h_x}{h} + (u_y + v_x)\frac{h_y}{h} \right] + \frac{\tau_x}{\rho_0 h}, \quad (8)$$

$$\frac{Dv}{Dt} + fv + g\frac{\partial h}{\partial y} = \nu \left[\nabla^2 v + (u_y + v_x)\frac{h_x}{h} - (u_x - v_y)\frac{h_y}{h} \right], \quad (9)$$

$$\frac{Dh}{Dt} + h\vec{\nabla} \cdot \vec{u} = 0. \quad (10)$$

182 Note that we added an Ekman forcing term τ_x/h due to the surface winds, which are modelled
 183 here as a body force.² The equations are normalized by total depth, rather than mean depth.

²Sometimes an Ekman layer is added above the explicitly modelled fluid layer. In that case the Ekman pumping appears in the h equation as well as the momentum equation (e.g., Pedlosky 1987b).

184 *d. Governing length scales*

185 In our simulations we pick the following physical parameters: $\tau = 0.1 \text{ N/m}^2$, $\rho_0 =$
 186 1000 kg/m^3 , $\beta = 2 \times 10^{-11}/(\text{ms})$, $f_0 = 1 \times 10^{-4}/\text{s}$, $L = 4 \times 10^6 \text{ m}$ and $H = 500 \text{ m}$. Our
 187 particular choice of layer depth is motivated by Rhines and Holland (1979), who find that
 188 for some oceanic flows the effect of the wind stress extends down to approximately 500 m.
 189 This means that our model describes the motion of a uniform-density surface layer with a
 190 free-surface and a flat bottom below to prevent any interaction with the ocean beneath.

The zonal and meridional domain is chosen such that $x \in [-L/2, L/2]$ and $y \in [-L/2, L/2]$.

With this choice we can set our wind stress to be

$$\tau_x = \tau_0 \sin\left(\frac{\pi y}{L}\right). \quad (11)$$

191 This means that the winds are strongest, and of equal magnitude, along the northern and
 192 southern boundaries. In the southern (northern) half of the domain the winds are westward
 193 (eastward). We emphasize that the wind stress is due to an imposed body force and we do
 194 not include any contribution from the ocean surface velocity (Duhaut and Straub 2006).

The Rossby radius of deformation (Pedlosky 1996) is a fundamental length scale that helps determine the dynamics of the flow. In the context of a barotropic model we have an external Rossby radius of deformation and it is,

$$L_R = \frac{\sqrt{gH}}{f_0}. \quad (12)$$

195 For our choice of parameters mentioned above $L_R = 700 \text{ km}$ or $k \approx 10^{-5}/\text{m}$. This length
 196 scale divides the gyre scale ($L > L_R$) and the mesoscale (for some range of $L < L_R$).³ The
 197 lower bound on the mesoscale is the submesoscale. In a stratified model we would also have
 198 internal radii of deformation that would be much smaller and would yield richer dynamics

³Depending on the mode in question, it is sometimes more appropriate to associate k_R with $1/L_R \approx 10^{-6}$ instead of $2\pi/L_R \approx 10^{-6}$. What is important here is that both of these wavenumbers are smaller than the others in the problem.

199 (Scott and Arbic 2007). A barotropic QG model can be seen as an asymptotic limit of
 200 our SW model about the mesoscale that ensures that the relative vorticity and the vortex
 201 stretching have the same relative importance.

In classical theories of wind-driven gyre flow the three boundary layers that can close the
 fluid transport across the basin are the Munk layer, Stommel layer and Charney (inertial)
 layer

$$\delta_M = \left(\frac{\nu}{\beta}\right)^{\frac{1}{3}}, \quad \delta_S = \frac{r}{\beta}, \quad \text{and} \quad \delta_I = \left(\frac{U_{wbc}}{\beta}\right)^{\frac{1}{2}}, \quad (13)$$

202 respectively (Pedlosky 1996). The Munk and Stommel layers both predict that the intensifi-
 203 cation must occur to the west since that is the only way that the vorticity added throughout
 204 the basin by the winds can be dissipated. The former is a lateral viscosity that parameterizes
 205 the effect of the sub-grid scale eddies that are not resolved. The latter is due to bottom drag
 206 and can be interpreted as due to unresolved turbulence below the ocean gyre. The Charney
 207 layer can balance the mass transport, but it does not predict any asymmetry between the
 208 west and east and therefore cannot be considered on its own (Ierley 1987). Note that for
 209 the inertial boundary layer we use the velocity scale of the WBC since it is dominant in
 210 the region of western intensification. Table 1 gives the values of these parameters for the
 211 different simulations described here.

In the introduction we defined the barotropic submesoscale, δ_{sm} , as the length scale that
 yields $Ro = O(1)$. If we use the velocity scale typical of the WBC this yields

$$\delta_{sm} = \frac{U_{wbc}}{f_0}. \quad (14)$$

212 In our turbulent simulation we have observed that $U_{wbc} \sim 1$ and therefore the barotropic
 213 submesoscale is approximately $L = O(10 \text{ km})$ or $k = 6 \times 10^{-4} / \text{m}$.

214 Therefore, we can view the dynamics of a wind-driven gyre as consisting of three distinct
 215 regimes: the synoptic (gyre) scale ($L > L_R$), the mesoscale ($\delta_{sm} < L < L_R$) and the
 216 submesoscale ($L < \delta_{sm}$). The gyre scale can be modelled using a planetary geostrophic model
 217 that accounts for the longitudinal variation of the Coriolis parameter (Pedlosky 1996). The

218 mesoscale is well-described by QG. There has been some success in using the semi-geostrophic
219 equations (Eliassen 1948) to study some aspects submesoscale processes (Thomas et al. 2008).
220 Even though the SW model is restrictive because it does not include baroclinic effects, it does
221 allow for the simultaneous inclusion of these three different regimes. Our study can therefore
222 be taken as complementary to that of Lévy et al. (2010), where the emphasis is on the
223 effects of stratification by the baroclinic submesoscale. At the submesoscale the hydrostatic
224 approximation may start to break down, but overall the SW model is more accurate for
225 studying wind-driven gyre flow than QG because it allows for unbalanced motions.

226 3. Time-series of the numerical simulations

227 Throughout, we focus on the effects of the Munk layer, but we must also include a
228 Stommel layer in order to ensure that the gyre reaches statistical equilibrium. We therefore
229 set the strength of the bottom drag such that $\delta_S = \delta_M/4$ so that inertial and lateral viscosity
230 are the dominate effects. The wind stress and the dissipation parameters then determine
231 the thickness of the inertial (Charney) layer δ_I .

232 The most viscous simulation has $\nu = 160,000 \text{ m}^2/\text{s}$ on a grid of 256^2 with a Munk layer
233 thickness of $\delta_M = 200 \text{ km}$. This solution tends to a laminar steady state and is very similar
234 to the solution of a linear Munk problem. We then consider a sequence of simulations where
235 the viscosity decreases by a factor of eight so that the Munk layer thickness is reduced by a
236 factor of two. We set the resolution to ensure that in the SW simulations there are seven grid
237 points per Munk layer thickness. Using equations (12) and (14) we compute the associated
238 inertial and submesoscale length scales. Observe that both these scales increase as lateral
239 viscosity decreases. The various parameters are summarized in Table 1.

240 The three lowest Reynolds number cases are all laminar, but are characterized by west-
241 ward propagating basin modes. The case with $L_M = 25 \text{ km}$ generates eddies, but they are
242 restricted to a very narrow strip along the northern part of the western boundary. The only

243 truly turbulent case is the last one, with a Reynolds number of 3190. (This is much smaller
244 than in the real ocean which have Reynolds numbers up to $O(10^{10})$.) In this simulation the
245 mesoscale is $O(200 \text{ km})$, similar to the length scale of oceanic barotropic vortices. The sub-
246 mesoscale is approximately half the size of Munk layer thickness, 7 km. In our simulations
247 we generate vortices $O(20 \text{ km})$ that are not strictly within the submesoscale regime, but they
248 should nevertheless include some ageostrophic effects.

249 *a. Numerical method*

250 We use a Fourier-basis pseudo-spectral method to solve the SW equations of motion.
251 No-normal flow and no-slip boundary conditions are imposed using a discrete sine transform
252 (DST) and the free-slip boundary condition is imposed using a discrete cosine transform
253 (DCT). We compute our equations on a staggered grid with N_x and N_y grid points in
254 the zonal and meridional directions, respectively, and $\Delta x = L/N_x$ and $\Delta y = L/N_y$. All
255 variables are de-aliased after each time step using the ‘two-thirds rule’ to remove those
256 modes with length-scales smaller than $3\Delta x$. We use the third-order Adams-Bashforth (AB3)
257 time integration scheme. The time step, Δt , is bounded by the Courant-Friedrichs-Lewy
258 (CFL) stability condition (Courant and Friedrichs 1967). The need for small time steps (to
259 resolve fast gravity waves) and fine spatial resolution (to resolve fine vortical structure in
260 the boundary layer) means that our simulations are computationally intensive. To improve
261 execution times we have parallelized our code using the FFTW library and MPI.

262 The numerical method for the QG model is essentially the same except that we use
263 a Chebyshev differentiation matrix to compute the zonal derivatives. This is because we
264 need to impose both zero Dirichlet and Neumann boundary conditions at the western and
265 eastern walls and there is no Fourier basis that does both simultaneously. For the turbulent
266 simulation with $L_M = 12.5 \text{ km}$ we use $N_y = 2048$, as before and $N_x = 512$. The reason for
267 the discrepancy is because the Chebyshev grid is tightly clustered near the boundary and
268 therefore we do not need as many grid points to achieve the same level of accuracy. This

269 does have the drawback that the interior flow is less well resolved but because the interior is
270 very smooth this does not create any problems. The fact that the simulations are so similar
271 shows that spectral methods achieve a high-order of accuracy throughout the domain.

272 *b. Structure of the WBC*

273 In Figure 1 we plot the zonal slice of the mean meridional velocity through the centre
274 of the gyre ($y = 0$) for both the SW and QG simulations. The means were computed from
275 days 100 to 700. There is excellent agreement between the two, which shows that the QG
276 accurately models the overall dynamics of the wind-driven gyre. For the QG profile we plot
277 the points to illustrate how closely clustered they are near the boundary. The SW simulation
278 achieves the same profiles with only seven points per Munk layer thickness. This plot also
279 shows the width of the Stommel and Munk boundary layers. It is evident that the Munk
280 layer accurately represents the width of the shear layer adjacent to the boundary in the
281 nonlinear regime. The mean profile of the WBC is rather asymmetric, but the width is
282 roughly 100 km which is similar to the Charney layer thickness. This result shows how the
283 width of the shear layer is set by the Munk layer thickness, but the overall width of the WBC
284 is set by the inertial boundary layer thickness. In a following subsection we will see that the
285 transition in the kinetic energy spectra occurs at a critical length scale between these two
286 scales that divides the mesoscale into two qualitatively different regimes.

287 *c. Time series of global properties*

288 We begin by comparing the evolution of certain global properties in the SW simulations.
289 Four subfigures in figure 2 depict the time series in the following quantities: a) the kinetic
290 energy (KE), b) the potential enstrophy defined in QG (EN_{qg}), c) the available potential
291 energy (APE) and the d) the potential enstrophy defined by SW theory (EN_{sw}). These are

292 defined in detail in equations (15), (16), (17) and (18), respectively,

$$KE = \frac{1}{2}\rho_0 \iint_A h(u^2 + v^2) dx dy, \quad (15)$$

$$EN_{qg} = \frac{1}{H} \iint_A (v_x - u_y)^2 dx dy, \quad (16)$$

$$APE = \frac{1}{2}\rho_0 g \iint_A \eta^2 dx dy, \quad (17)$$

$$EN_{sw} = \iint_A \frac{(v_x - u_y + f)^2}{h} - \frac{f^2}{H} dx dy. \quad (18)$$

293 Note that we use a slightly unconventional definition of enstrophy: we normalized the QG
 294 enstrophy by H and the SW enstrophy includes only the fluctuating part of the enstrophy.
 295 We made these choices in order to facilitate comparisons between the two rather different
 296 expressions for enstrophy.

297 Figure 2(a) shows that the total kinetic energy in the wind-driven gyre changes dramati-
 298 cally with respect to the amount of dissipation. In all the simulations the kinetic energy
 299 increases exponentially as the gyre spins up and then saturates due to the nonlinear ad-
 300 vection. The most viscous (also laminar) simulation equilibrates early and with relatively
 301 little energy in comparison to the turbulent simulation. Reducing the viscous boundary
 302 layer thickness by a factor of 10 increases the spin up time by a similar factor: 30 days for
 303 $L_M = 200$ km compared to 300 days for $L_M = 12.5$ km. As well, the amount of kinetic energy
 304 contained in the gyre increases by over an order of magnitude. Initially in this investigation
 305 we ran these simulations without any bottom drag. The equilibration levels were similar
 306 for the viscous runs but the turbulent case never equilibrated, even after 1000 days. The
 307 bottom drag is essential because we wish to study the energy spectra and associated energy
 308 transfers in an equilibrated system.

309 Figure 2(b) shows that in all cases the QG potential enstrophy increases exponentially
 310 at first and then saturates to reach statistical equilibrium, albeit slightly sooner compared
 311 to the kinetic energy. The QG simulations behave similarly (results not shown here), and
 312 the spin up times and the equilibrium levels of both the KE and EN_{qg} are well described
 313 by the QG dynamics. However, the details of the oscillations about the mean differ between

314 QG and SW because the characteristics of QG and SW turbulence differ.

315 The plot of available potential energy (APE), figure 2 (c), does not have an analogue
316 in our QG simulation because we have taken the limit of a rigid lid. In these plots we see
317 that the the APE stored in the wind-driven gyre increases with decreasing viscosity. In
318 each case a maximum of potential energy is achieved within the first ten days. The systems
319 then overshoot their equilibrium levels and then the APE decreases, subsequently yielding
320 oscillations. In the laminar cases the saturation level is essentially flat because the system is
321 near steady state. The two simulations that generate eddies experience fluctuations about
322 the equilibrium level. The turbulent solution actually increases its APE quite significantly
323 in a rather erratic manner. The details of this curve are set by the complex nonlinear
324 interactions.

325 Figure 2(d) shows the SW potential enstrophy, a quantity that is conserved in the absence
326 of forcing and dissipation, unlike the QG potential enstrophy mentioned above. In all the
327 simulations this field attains a local minimum in the first ten days. The potential enstrophy
328 increases significantly only after the vortices have been generated. Indeed, the potential
329 enstrophy level seems to depend on the level of turbulence generated in the basin.

330 In order to test the accuracy of our results we ran a numerical simulation with exactly the
331 same parameters as our turbulent SW run but with twice the resolution, $N_x = N_y = 4096$.
332 To evolve the solution to day 200 took several months of computing on 128 processors and
333 the plots of the time series are virtually identical. This shows that our numerical results
334 have converged globally.

335 4. Energy spectra

336 *a. Methodology*

337 Computing the energy spectra in a periodic domain is relatively easy because we can take
338 the transforms of the fields directly. The presence of a solid boundary complicates matters.

339 Capet et al. (2008b) and Fischer and Bruneau (2009) overcame this hurdle by using a window
 340 to convert the field to one that is periodic. This is undesirable for our study because a window
 341 would remove a significant portion of the WBC, which is an essential feature that we want
 342 to investigate. It is for this reason that we have decided instead to compute energy spectra
 343 using spectral extensions. By that we mean that we extend the primitive variables u, v, η
 344 in either an odd or even way, depending on the boundary conditions to obtain fields that
 345 are strictly periodic. The fields with zero Dirichlet (Neumann) boundary conditions use the
 346 the odd (even) extension, which is essentially equivalent to using the Discrete Sine (Cosine)
 347 Transform.

Subsequently, we compute the two-dimensional FFT of these extended solutions and integrate the square of the modulus over rings of equal wavenumber modulus $k = |\vec{k}|$ to determine the spectral distribution of each of these variables: $|\hat{u}|^2, |\hat{v}|^2, |\hat{\eta}|^2$. The sum of the first two yields the spectral kinetic energy density and the third is the spectral potential energy density:

$$E_{KE}(k) = \int_0^{2\pi} \int_{k-\frac{dk}{2}}^{k+\frac{dk}{2}} |\hat{u}|^2 + |\hat{v}|^2 dA,$$

$$E_{PE}(k) = \int_0^{2\pi} \int_{k-\frac{dk}{2}}^{k+\frac{dk}{2}} |\hat{\eta}|^2 dA.$$

348 Note that we follow convention and use hats to denote transformed fields.

349 One issue that we must address is that the kinetic energy of the SW model is defined
 350 to be the depth integral of the kinetic energy in each level $\frac{1}{2}h(u^2 + v^2)$. This quantity is
 351 problematic in that it is cubic and thus we cannot apply traditional methods (Warn 1986).
 352 It is for this reason that we choose to look at the KE at each depth, which is uniform for all
 353 depths and thus it is simpler and unambiguous. We restrict our attention to the unfiltered
 354 modes (wavenumbers below the 2/3-rule cut-off), since those are the ones of physical interest.

355 We complement the standard Fourier-based spectral analysis with wavelet analysis to
 356 compute energy spectra and spectral fluxes. The wavelet approach allows us to use a log-
 357 arithmic distribution of wavenumbers to better resolve the behaviour at large scales and

358 produces smoother spectra that are easier to interpret. Furthermore, we use the Wavelet
359 analysis to calculate local spectra in turbulent and laminar regions and contrast them to the
360 average spectrum over the whole gyre. For a detailed review of wavelet analysis techniques
361 for turbulent flows the reader should consult Farge (1992); Farge et al. (1996). Our wavelet
362 analysis uses an isotropic version of the two-dimensional 8th-order Cauchy wavelet proposed
363 by Antoine et al. (1999). Results are normalized such that the wavelet and Fourier spectra
364 have the same total energy.

365 *b. Energy spectra of total fields*

366 In both the SW and QG turbulent simulations the increase in kinetic energy saturates
367 after 300 days and subsequently enters a state of statistical equilibrium. In this regime it
368 is of interest to compute the power spectrum of the kinetic energy to learn how the energy
369 is distributed amongst the different scales. In the subsequent subsection we investigate how
370 this spectrum is maintained by computing explicitly the spectral transfer and fluxes.

371 Figure 3 shows five different wavelet power spectra of the total solution azimuthally
372 integrated in spectral space and time integrated over days 300 to 305. Because there was
373 not much variation in this field it was deemed unnecessary to integrate over a wider interval
374 of time. We compute spectra for the kinetic energy (KE), available potential energy (APE),
375 kinetic energy in the QG simulation (QG), and zonal (u) and meridional (v) velocities.
376 Superimposed on this plot are two straight lines with slopes $-5/3$ and -5 which approximate
377 the slopes of kinetic energy in different regimes. Note that the spectra of the velocities are
378 all shifted downwards to separate them from the other curves.

379 The spectrum of the kinetic energy is complex, but can be understood by considering
380 each dynamical regime separately. The synoptic scale is larger than the external radius of
381 deformation, $k < 10^{-5}/\text{m}$, the mesoscale lies between $10^{-5} < k < 6 \times 10^{-4}/\text{m}$ and the
382 submesoscale is to the far right, $k > 6 \times 10^{-4}/\text{m}$. The mesoscale is divided into two distinct
383 regions at $k = 10^{-4}$ where the slope of the energy spectrum changes. At large scales spectral

384 slopes of KE are close to $k^{-5/3}$, which suggests there is an inverse cascade of energy as in the
385 Batchelor–Leith–Kraichnan theory of unbounded two-dimensional turbulence. This range
386 spans nearly a decade and there is very good agreement between the spectra of KE in the
387 SW run and its corresponding APE. In the QG limit the free-surface height is precisely the
388 streamfunction for the horizontal velocity and multiplying the integrated power spectrum of
389 the APE by k^2 yields the power spectrum in the same units as the kinetic energy. Therefore,
390 if we compare the power spectra of the kinetic energy and the APE we measure how similar
391 the SW dynamics are to the QG dynamics. Deviation between the KE and APE curves
392 indicates a break in geostrophic balance.

393 The spectrum for the QG KE is nearly parallel to the SW KE in this range. One subtle
394 difference is that around 300 km the QG energy spectrum has a local maximum, in contrast
395 to the SW which has a local minimum. This indicates that at this time the QG simulation
396 has more energy at this length scale compared to the SW analogue. Indeed, the vorticity
397 field of the QG simulation has several vortices of this size whereas the SW analogue has a
398 wider range of vortical sizes.

399 Also, at the larger part of the mesoscale both components of velocity are comparable and
400 contribute to the overall spectrum. This is in contrast to the relatively smaller length scales
401 where it is evident that the meridional velocity is the dominant component. This occurs
402 because the former is dominated by eddies whereas the latter is predominantly controlled
403 by the strong meridional WBC.

404 There is a kink on the order of the inertial scale, $k = 10^{-4}$, where all the energy spectra
405 curves change their slope. This is the length scale where energy is injected into the system
406 and is due to the width of the WBC, which then sets the typical size of the eddies that are
407 generated by the barotropic instability of the jet. These eddies then interact in a nonlin-
408 early to generate an inverse energy cascade to larger scales, as is typical in two-dimensional
409 turbulence. These interactions naturally generate filaments, which causes enstrophy to be
410 transferred to smaller scales. The mesoscale motions with smaller horizontal wavelengths

411 all have energy spectra that are steeper, smoother and slopes that are nearly linear. The
412 slopes of the energy spectra in this range all differ slightly. The steepest is the QG KE and
413 the shallowest is the PE. Note that in the QG model has linear Laplacian viscosity in the
414 vorticity equation, whereas the SW model has nonlinear lateral viscosity and no diffusivity
415 in the continuity equation. The fact that these are different could explain these different
416 slopes. Tran and Shepherd (2002) established theoretically that, depending on the type of
417 dissipation used, the enstrophy cascade range of scales can have a spectral slope between
418 -3 and -5 . However, the nonlinear dissipation in the SW simulations was not one they
419 considered and therefore we cannot directly apply their theory. Figure 3 shows that the
420 spectral slopes of the kinetic and available potential energies are both close to -5 . These
421 results are consistent with the theoretical predictions and numerical simulations of forced
422 two-dimensional turbulence.

423 There are clearly many similarities between our relatively complex model of wind-driven
424 gyre flow and numerical simulations of two-dimensional turbulence. In the latter, forcing
425 injects energy over a narrow range of wavenumbers (so-called monoscale forcing). The length
426 scale of the WBC is analogous to this forcing scale since it determines the size of the eddies
427 that are produced. It is for this reason that we get an overall picture that is qualitatively
428 similar to forced two-dimensional turbulence. Indeed, the random variations in the forcing of
429 the idealized problem could be seen as parameterizing the variable eddy sizes and strengths
430 that are generated due to the strong shear in the WBC. However, we emphasize that in our
431 problem the forcing is due to wind stress that indirectly forces the gyre at much smaller
432 scales between of the return flow along the western boundary. This investigation, albeit in
433 a rather idealized setting, helps to bridge the gap between classical simulations of forced
434 two-dimensional turbulence and the real dynamics of wind-driven gyres.

435 In the synoptic scale the KE and APE spectra differ dramatically in form, which signifies
436 strong deviation from geostrophic balance. The KE of the SW and QG are similar but they
437 do have some notable differences, which is not surprising because QG is not strictly valid

438 on these scales where planetary geostrophic balance should hold to leading order (where the
439 variations in the Coriolis term is important). We emphasize that the fine structure that we
440 observe at large scales is only visible using the wavelet-based method, which allows us to
441 choose logarithmically distributed wavenumbers.

442 The transition from the small mesoscale to the barotropic submesoscale is subtle. Almost
443 all the spectral curves maintain the same slope, except for the PE. This spectrum becomes
444 very shallow, which shows that there is relatively more energy at this scale and that the
445 dynamics in this regime is ageostrophic. Unfortunately, these details cannot be resolved by
446 the current simulation will be investigated in future work.

447 *c. Energy spectra of perturbation fields*

448 Next, we compute the corresponding energy spectra of the perturbations about the mean
449 state in order to try to better understand the dynamics of the fluctuations. The same five
450 spectra shown in the previous figure are presented in Figure 4. We analyze the equilibrium
451 dynamics by considering the three different dynamical scales. In the synoptic range all
452 the energy spectra have a predominantly positive slope because of the spectral peak that
453 occurs at the external radius of deformation. This energy build up occurs because there is
454 a predominance of eddies that have a length scale similar to, or slightly smaller than, that
455 of the Rossby radius. Since QG is designed to describe this regime it is not surprising that
456 it accurately captures the dominant features of wind-driven gyre flow. Again, we see that
457 the spectra corresponding to the kinetic energy and the APE are nearly parallel, indicating
458 there is a near geostrophic balance for these motions.

459 The slope of the kinetic energy spectra in the large mesoscale range is similar to -3 ,
460 as predicted for freely evolving two-dimensional turbulence. Note that there is not as large
461 region of a shallower slope, e.g., $-5/3$ as in the total kinetic energy. This is because the
462 forcing and much of the damping is confined to the mean state. In the short mesoscale range
463 we find that the kinetic energy spectra has a slope similar to -5 , as in the previous case.

464 The spectra of the APE is even shallower still, once again indicating deviations from QG
465 dynamics. This extends into the submesoscale regime, as is suggested by the fact that there
466 is still the same shallowing of the slope at the smallest scales. This figure also shows that
467 the energy spectrum in the QG simulation closely resemble its SW analogue. The largest
468 differences occur in the synoptic scales where the QG spectrum decreases much more rapidly
469 at larger scales.

470 *d. Localizaton of Spectra*

471 To conclude this section we exploit a characteristic of the wavelet transform in that it can
472 show how the kinetic energy spectra can vary locally in space. Subplots: a) and b) in Figure
473 5 depict the vorticity of the QG and SW simulations, respectively, at day 300 well after
474 the unstable WBC has generated turbulence in the north-western corner. There is a white
475 square of size $1,000 \text{ km} \times 1,000 \text{ km}$ in each that isolates a region of turbulence (1/4 the total
476 size of the domain) away from the WBC. As well, subplots c) and d) show different spectra
477 for the QG and SW simulations. Each presents three spectra: 1) the Wavelet spectrum
478 that is integrated over the entire domain, 2) the Wavelet spectrum in a subdomain of the
479 south-western quadrant that is laminar (not shown here) and 3) the Wavelet spectrum in the
480 white domain depicted above where the flow is turbulent and does not contain the WBC.

481 It is readily observed from subplots a) and b) that even though both simulations are
482 turbulent the details of the flow differ significantly. It is very difficult to quantify these
483 differences using the vorticity plots. One means of quantifying the characteristic differences
484 of the turbulence is to compare the energy spectra, what we present in subplots c) and d).
485 The Fourier transform (not shown here) and the Wavelet transform, in (c) and (d), integrated
486 over all the scales produce spectra that are very similar. There are some minor differences
487 on the largest scales and the Wavelet spectrum is much smoother, which is typically the
488 case. The spectra in the south-eastern domain is strongest at the largest scale due to the
489 Sverdrup flow that exists but then quickly decays just beyond the Rossby radius. The

490 spectra in the turbulent subdomain in the north-western quadrant is more interesting. Both
491 the QG and SW spectra are very similar on the planetary scale and mesoscale but there
492 are significant differences that occur in the smaller part of the mesoscale. The localized
493 spectra in the turbulent region seems to have 3 spectral ranges: 1) near the Rossby radius
494 there is a narrow regime that is a bit steeper than $-5/3$, 2) starting at the Charney scale the
495 slope seems to change to -4 , and 3) near the Munk scale we have that the slope changes
496 to something closer to -7 . The first regime is attributed to the inverse energy cascade,
497 the second could be due to the direct enstrophy cascade and the final regime should be
498 due to the dissipative range. The associated QG spectra differ in that the spectral range
499 of -4 extends for a much wider range of scales. Therefore, we surmise that even though
500 the global spectra agree remarkably well, the localized spectra differ significantly near the
501 Charney scale where nonlinear effects play an essential role in the evolution of the gyre, and
502 the asymmetry between cyclonic and anticyclonic eddies in SW is likely to deviate from QG.
503 We remark that we also used a Tukey window combined with the Fourier transform and also
504 found the three distinct regimes in the SW simulations.

505 **5. Spectral energy transfers**

506 In this section we investigate how the energy is transferred between length scales due
507 to the various terms in the momentum equation. We follow the methodology presented in
508 Scott and Arbic (2007), Capet et al. (2008b) and Lesieur (1997). Unlike the energy spectra,
509 the spectral transfers (and fluxes) vary significantly in time and must therefore be averaged
510 over many different realizations. Preliminary results indicate few differences between the
511 transfers computed by the Fourier and Wavelet methods, however, a substantial reduction
512 in computational costs is gained from the former. Therefore, we have chosen to use the
513 Fourier approach to compute the energy transfers in our simulations. Results are averaged
514 from day 300 to day 700.

515 A statistically stationary forced two-dimensional turbulent fluid in a doubly periodic or
 516 unbounded domain is expected to have an inverse energy cascade to larger scales for scales
 517 larger than the forcing scale (without scale to scale transfer of enstrophy) and an enstro-
 518 phy cascade (without scale to scale transfer of energy) from the forcing scale to smaller
 519 scales (Kraichnan 1967). However, in the forced-dissipative basin flow, this cannot be con-
 520 sistent with the large scale energy forcing. Scott and Straub (1998) studied a similar problem
 521 to the one we consider here, but only in the QG regime. They determined that for constant
 522 forcing and small viscosity, the wind energy input must decrease to satisfy global energy
 523 conservation in order to guarantee that the Rossby number remains small. An equivalent
 524 behavior occurs in vorticity forcing Fox-Kemper (2005). As well, Scott and Arbic (2007)
 525 investigated a similar forced-dissipative system with a two-layer baroclinic QG model. This
 526 differs from ours in two ways: their forcing is a baroclinically unstable shear flow that forces
 527 the motion at the internal radius of deformation, and the damping is primarily due to a
 528 bottom drag.

529 *a. Methodology*

To derive the equation that governs the evolution of the spectral density transfer we
 transform the SW momentum equation, multiply the resulting equation by the conjugate of
 the transform of the velocity $\hat{\mathbf{u}}^*$ and then adding the resultants. This yields an evolution
 equation for the spectral density,

$$\frac{\partial}{\partial t} \left(\frac{1}{2} \hat{\mathbf{u}}^* \hat{\mathbf{u}} \right) = -\text{Re} \left[\hat{\mathbf{u}}^* \cdot \left(\widehat{\mathbf{u} \cdot \nabla \mathbf{u}} \right) + \hat{\mathbf{u}}^* \cdot \left(\widehat{\hat{k} \times \mathbf{u}} \right) + \hat{\mathbf{u}}^* \cdot \widehat{g \nabla h} \right] + \text{Re} \left[\hat{\mathbf{u}}^* \cdot \widehat{\mathbf{F}} \right]. \quad (19)$$

530 If we average a statistically stationary solution over many days we expect the left hand
 531 side to be approximately zero. The spectral (turbulent) transfer has contributions from
 532 nonlinear advection, the Coriolis force, hydrostatic pressure and external forcing by the
 533 winds and dissipation, both lateral viscosity and bottom drag. In contrast to Nadiga and
 534 Straub (2010) we plot each contribution separately rather than summing terms together.

535 Throughout, we only consider the unfiltered wavenumbers below the 2/3 cut-off.

Similarly, to compute the transfer in the APE we multiply the transformed continuity equation in the SW model by the complex conjugate of the transformed depth to obtain an equation for the spectral transfer of potential energy,

$$\frac{\partial}{\partial t} \left(\frac{1}{2} \hat{\mathbf{h}}^* \hat{\mathbf{h}} \right) = -\text{Re} \left[\hat{\mathbf{h}}^* \widehat{\nabla \cdot (h\mathbf{u})} \right]. \quad (20)$$

536 We computed the spectral transfer of APE and found that even though it is generally non-
537 zero at a given instant, the average mean flux is approximately zero. This shows that
538 although there is instantaneously spectral transfer between kinetic and potential energy, on
539 average this transfer is very small and we therefore do not present these results.

540 There are two obvious approaches to determine the spectral transfers and fluxes of the
541 kinetic energy in the QG model. The conventional method, as is used in Scott and Arbic
542 (2007) and Nadiga and Straub (2010), is to compute the transform of the PV equation and
543 multiply this by the conjugate transform of the streamfunction. Alternatively, equation (19)
544 can be obtained from the momentum equation, as before. The complication is that the
545 pressure is not directly available from the numerical simulations. However, computation of
546 the nonlinear spectral transfer, usually referred to as T_k , does not require the pressure field.

547 As with the energy spectra, we use spectral extensions instead of windowing since it
548 preserves the structure within the WBC. It is important to extend the equations in such a
549 way that the equations are satisfied in each quadrant, otherwise there is no reason to assume
550 that the fluxes will actually balance. In particular, for all the terms in the x -momentum
551 equation we extend the fields in an odd way in the zonal and an even way in the meridional.
552 In the y -momentum equation we extend the terms in an odd way in both directions and
553 for the continuity equation we extend all the terms in an even way in both directions.
554 Unfortunately, there are some terms that do not share the same boundary conditions and
555 this has produced some error due to boundary discontinuities.

556 *b. Spectral Fluxes of turbulent simulations*

557 In figure 6 we present both the spectral transfers and fluxes for the wind forcing, lateral
558 viscosity and bottom drag. These are distinct from the other three mechanisms in that they
559 have a net spectral flux throughout the basin. Note that in Figure 6 (a) the dissipative
560 terms are rescaled by a factor of 100 because they are much weaker than the winds and
561 otherwise would not otherwise be visible. This figure confirms our intuition about which
562 spectral transfers arise because of the external forces. First, the wind inputs energy only at
563 the very largest scale. Secondly, the lateral viscosity dissipates more energy compared to the
564 bottom drag. This is to be expected because the Stommel layer is much narrower than the
565 Munk layer. Thirdly, lateral viscosity is strongest near the Charney scale where the eddies
566 are generated and then decays at larger scale (where it is not an effective means of removing
567 energy) and at smaller scales where this is little energy to dissipate. This is in contrast to
568 the bottom drag that is very strong at the basin scale and also the Rossby radius since these
569 are the two scales that contain most energy.

570 The transfers (and fluxes) of the terms that have no net contribution are presented in
571 subplots (a) and (b) in Figure 7. The Coriolis and pressure terms create a direct cascade of
572 energy from the gyre scale to smaller scales. In the mesoscale we see that they are nearly
573 mirror images of each other, again because geostrophic balance holds to leading order. It is
574 interesting to note that there are oscillations in these curves in the mesoscale regime that
575 indicate there is a rather complex transfer of spectral energy across scales. The effect of the
576 nonlinear advection is rather different and will be addressed in the discussion of the next
577 figure.

578 In Figure 8 we compare the spectral transfer (and fluxes) of the nonlinear advection in the
579 SW and QG simulations. Qualitatively, the two simulations are in good agreement. They
580 confirm that there is a strong inverse energy cascade that increases the energy at the gyre
581 scale due to vortex mergers. As is evident from the spectral flux, there is also a relatively
582 weak direct energy cascade around the Charney scale. This direct cascade is reminiscent of

583 the simulations of reduced gravity dynamics in Zhai et al. (2010) and is also believed to be
584 due the effect of the western boundary. On closer examination, it appears that the spectral
585 flux at the submesoscale extends down to the grid scale with a magnitude of $O(10^{-18})$ for
586 both the QG and SW runs. However, the basic assumptions of QG are violated in this regime
587 since the Rossby number is order one. In contrast, the SW model accurately describes the
588 barotropic motions at this scale as long as the hydrostatic approximation is not violated.

589 The spectral transfers are also highly oscillatory in the mesoscale regime, but there are
590 some clear differences between the QG and SW models. Both have a very strong positive
591 peak, indicating that large amounts of energy are transferred to the external Rossby radius of
592 deformation. However, the peak is larger and narrower in the SW regime. These differences
593 are also visible in the spectral flux. We attribute this to the fact that the SW model is more
594 sensitive to how the dynamics change at different length scales.

595 The strong indirect and weak direct energy cascades described above were previously
596 observed in Nadiga and Straub (2010) in the context of the double gyre in a one layer QG
597 model. Here we have confirmed that these effects are also present in the SW regime and
598 emphasize that the details at the submesoscale are better described by the SW model. Our
599 simulation results are very similar to their case G2. One distinction is that they find that
600 the spectral flux due to nonlinear advection at the synoptic scale is positive, whereas we find
601 that it is negative. When we computed the spectral transfers in the QG using the vorticity
602 formulation we found curves very similar to theirs. It is unclear to us why there is this
603 discrepancy in the two methods, but believe that it is likely due to the aperiodicity of the
604 gyre and the way in which the flows are extended in the two different formulations.

605 **6. Conclusions**

606 We have revisited the classical problem of barotropic wind-driven gyre flow, comparing
607 the results of QG and SW simulations. The novelty of our approach lies in our ability to

608 resolve the gyre scale, mesoscale and, at least partly, the submesoscale dynamics using the
609 SW model. We have shown that there is a unique choice to model the vital effect of lateral
610 friction that follows from reducing the viscous term in the three-dimensional equations of
611 motion to the hydrostatic, two-dimensional limit. The resulting dissipation is nonlinear, but
612 should be more accurate in its effect on the small scale motions.

613 To analyze the kinetic and potential energy spectra we have used a wavelet-based ap-
614 proach. Because this method is very slow we instead used a Fourier based method to com-
615 pute the spectral transfers and fluxes. When integrated over the entire domain the Wavelet
616 method yields the same spectra as that obtained from the classical approach, however it
617 produces smoother spectra and allows for better resolution of the large scales. Furthermore,
618 we have presented the wavelet spectra for the SW and QG simulations integrated over a
619 turbulent region away from the WBC. This revealed that the SW model has three distinct
620 dynamical regions in comparison to QG that only has one. The reason why the global spec-
621 tra are so similar is because the mean WBC, which is the most energetic feature in the basin,
622 is almost identical in the two models.

623 We have fully quantified the energy cascade in the SW model, since it more accurately
624 resolves the entire range of active scales than the QG model. When the sub-grid scale
625 viscosity is sufficiently small we simulated the dynamics of a turbulent WBC. The power
626 spectrum of the total kinetic energy has a shallow $-5/3$ scaling in the mesoscale regime
627 because of the strong inverse energy cascade. Then for smaller scales there is a transition
628 at the Charney scale where the spectrum becomes -5 , that is attributed to the viscous
629 forces that are dominant near the grid scale. This dual power-law spectrum is consistent
630 with simulations of forced two-dimensional turbulence using the Navier–Stokes equations,
631 although the underlying equations are different and the wind-stress forcing in our simulations
632 is more physically realistic. In the barotropic submesoscale regime the PE spectrum is
633 much shallower than that consistent with geostrophy, which indicates a break of geostrophic
634 balance, as is typical of submesoscale motions. The spectral fluxes confirmed that there

635 is a strong inverse energy cascade, but also showed a weaker direct energy cascade that
636 extends down to the grid scale. This small direct energy cascade is significant since in
637 the oceans energy must be eventually transferred to the smallest, three-dimensional, scales.
638 Even though this direct energy cascade occurs in both the QG and SW simulations, it is
639 only accurately described in the SW model.

640 Of particular interest here is the interplay of the range of scales where the potential
641 enstrophy cascade -3 slope occurs. In the doubly-periodic case, this cascade only occurs in
642 exclusion of the energy cascade in either direction. It has been hypothesized that western
643 boundary currents or submesoscale dynamics might allow some variation in this story. The
644 boundaries do seem to have some effect, as there is a weak forward energy cascade over
645 the same range of scales as the -3 spectral slope. Intriguingly, this result occurs in QG,
646 (consistent with Nadiga and Straub 2010), but barotropic submesoscale dynamics do not
647 appreciably enhance this forward cascade. While loss of balance or radiation of gravity
648 waves can occur here, these effects are negligibly weak in terms of energy flux.

649 A highlight of our work is the important role boundaries play in determining spectral
650 energy transfers. In two-dimensional simulations of turbulence it is well established that QG
651 turbulence in a periodic domain predominantly transfers energy to large scales and cannot
652 generate a significant direct energy cascade. However, in the presence of a solid boundary,
653 the conservation of mass forces a strong return flow along the western boundary, the size of
654 which is determined by the sub-grid scale viscosity. Strong, narrow, WBCs can be viewed
655 as injecting energy at scales larger than the Munk boundary layer width, which can then be
656 transferred to large scales by two-dimensional turbulence. This modifies the different energy
657 spectra and spectral fluxes because the SW model is more sensitive to the changes in the
658 length scale of the flow than the QG model.

659 This research has established the machinery to accurately resolve a wide range of length
660 and time scales in geophysical flows. As a first step we focused on a barotropic SW model
661 because of its historical significance and the fact that every ocean model possesses a barotropic

662 mode. Future work will extend this investigation by introducing three important features:
663 stratification, topography and realistic winds, since they are well known to alter the ki-
664 netic energy transfer in currents such as the WBC (Poulin and Flierl 2005; Poulin 2010;
665 Poulin et al. 2010). Introducing realistic coastlines is desirable, but problematic because
666 our methodology does not extend well to non-rectangular domains. Using a wavelet-based
667 method along with an adaptive grid is a powerful approach that is currently being developed.
668 We hope that this research programme will improve our understanding of the interaction be-
669 tween the mesoscale and submesoscale, and thereby aid in the development of more accurate
670 parameterizations for climate and weather models.

671 Acknowledgements : FJP and NKRK would like to thank NSERC for financial support
672 during the research and writing of this manuscript, Compute-Canada for the computing
673 resources to perform these calculations and Laboratoire Météorologie Dynamique in Paris
674 for Sabbatical Fellowships they received in 2011. FJP would also like to thank CIRES
675 for a Sabbatical Fellowship to visit the University of Colorado at Boulder, Pascale Lelong,
676 Jonathan Lilly, Peter Rhines and Michael Waite for helpful discussions throughout. BFK
677 was supported by NSF 055010 and NSF 005614.

678

679 REFERENCES

- 680 Antoine, J.-P., R. Murenzi, and P. Vandergheynst, 1999: Directional wavelets revisited:
681 Cauchy wavelets and symmetry detection in patterns. *Appl. Comput. Harmon. Anal.*,
682 **6 (3)**, 314–345.
- 683 Boccaletti, G., R. Ferrari, and B. Fox-Kemper, 2007: Mixed layer instabilities and restrati-
684 fication. *J. Phys. Oceanogr.*, **37**, 2228–2250.

- 685 Capet, X., J. McWilliams, M. Molemaker, and A. Shchepetkin, 2008a: Mesoscale to subme-
686 soscale transition in the california current system. part I: Flow structure, eddy flux, and
687 observational tests. *J. Phys. Oceanogr.*, **38**, 29–43.
- 688 Capet, X., J. McWilliams, M. Molemaker, and A. Shchepetkin, 2008b: Mesoscale to subme-
689 soscale transition in the california current system. parti III: energy balance and flux. *J.*
690 *Phys. Oceanogr.*, **38**, 2256–2269.
- 691 Carton, X., 2000: Hydrodynamical modeling of oceanic vortices. *Surveys in Geophys.*,
692 **22 (3)**, 179–263.
- 693 Charney, J., 1955: The gulf sream as an inertial boundary layer. *Proc. Nat. Acad. Sci.*, **41**,
694 731–740.
- 695 Clercx, H. and G. van Heijst, 2009: Two-dimensional navier-stokes turbulence in boudned
696 domains. *Applied Mech. Rev.*, **62**, 020 802–1 020 802–25.
- 697 Courant, R. and H. Friedrichs, K adn Lewy, 1967: On the partial difference equations of
698 matheamtical physics. *IBM Journal*, **11**, 215–234.
- 699 Duhaut, T. and D. Straub, 2006: Wind stress dependence on ocean surface velocity: impli-
700 cations for mechanical energy input to ocean circulation. *J. Phys. Oceanogr.*, **36**, 202–211.
- 701 Eliassen, A., 1948: The quasi-static equations of motion. *Geofys, Publikasjoner*, **17 (3)**.
- 702 Farge, M., 1992: Wavelet transforms and their applications to turbulence. *Annu. Rev. Fluid*
703 *Mech.*, **24**, 395–457.
- 704 Farge, M., N. K.-R. Kevlahan, V. Perrier, and E. Goirand, 1996: Wavelets and turbulence.
705 *IEEEE Proceedins, Special issue on Wavelets, et. I Daubechies and Kovasevic*, **84 (4)**,
706 639–669.
- 707 Fischer, P. and C.-H. Bruneau, 2009: Wavelet-based analysis of enstrophy transfers in two-
708 dimensional turbulence. *Phys. Fluids*, **21**, 065 109–1 065 109–11.

709 Fox-Kemper, B., 2004: Wind-driven barotropic gyre II: Effects of eddies and low interior
710 viscosity. *Journal of Marine Research*, **62** (2), 195–232, doi:10.1357/002224004774201690.

711 Fox-Kemper, B., 2005: Reevaluating the roles of eddies in multiple barotropic wind-driven
712 gyres. *Journal of Physical Oceanography*, **35** (7), 1263–1278, doi:10.1175/JPO2743.1.

713 Fox-Kemper, B. and R. Ferrari, 2008: Parameterization of mixed layer eddies. Part II:
714 Prognosis and impact. *Journal of Physical Oceanography*, **38** (6), 1166–1179, doi:10.1175/
715 2007JPO3788.1.

716 Fox-Kemper, B., R. Ferrari, and R. W. Hallberg, 2008: Parameterization of mixed layer
717 eddies. Part I: Theory and diagnosis. *Journal of Physical Oceanography*, **38** (6), 1145–
718 1165, doi:10.1175/2007JPO3792.1.

719 Fox-Kemper, B. and J. Pedlosky, 2004: Wind-drive barotropic gyre I: Circulation control by
720 eddy vorticity fluxes to an enhanced removal region. *J. Mar. Res.*, **62**, 169–193.

721 Fox-Kemper, B., et al., 2011: Parameterization of mixed layer eddies. III: Implementation
722 and impact in global ocean climate simulations. *Ocean Modelling*, in press.

723 Gent, P., 1993: The energetically consistent shallow-water equations. *J. Atmos. Sci.*, **50** (9),
724 1323–1325.

725 Grooms, I., K. Julien, and B. Fox-Kemper, 2011: On the interactions between planetary
726 geostrophy and mesoscale eddies. *Dynamics of Atmospheres and Oceans*, in press.

727 Holland, W., 1978: The role of mesoscale eddies in the general circulation of the ocean—
728 numerical experiments using a wind-driven quasi-geostrophic model. *J. Phys. Oceanogr.*,
729 **8** (3), 363–392.

730 Hosegood, P., M. C. Gregg, and M. H. Alford, 2006: Sub-mesoscale lateral den-
731 sity structure in the oceanic surface mixed layer. *J. Geophys. Res.*, **33** (L22604),
732 doi:10.1029/2006GL026797.

- 733 Jerley, G., 1987: On the onset of recirculation in barotropic general circulation models. *J.*
734 *Phys. Oceanogr.*, **17** (29), 2366–2374.
- 735 Kevlahan, N. K.-R. and M. Farge, 1997: Vorticity filaments in two-dimensional turbulence:
736 creation, stability and effect. *J. Fluid Mech.*, **346**, 49–76.
- 737 Kraichnan, R., 1967: Inertial ranges on 2-dimensional turbulence. *Phys. Fluids*, **10**, 1417–23.
- 738 Kraichnan, R. and D. Montgomery, 1980: Two-dimensional turbulence. *Rep. Prog. Phys.*,
739 **43**, 547–619.
- 740 Kundu, P. and I. Cohen, 2008: *Fluid Mechanics*. Elsevier.
- 741 Lesieur, M., 1997: *Turbulence in Fluids*, Fluid Mechanics and Its Applications, Vol. 40. 3d
742 ed., Kluwer Academic Publishers.
- 743 Lévy, M., P. Klein, A. M. Tréguier, D. Iovino, G. Madec, S. Masson, and K. Takahashi, 2010:
744 Modifications of gyre circulation by sub-mesoscale physics. *Ocean Modelling*, **34** (1-2),
745 1–15.
- 746 McClean, J. L., et al., 2011: A prototype two-decade fully-coupled fine-resolution ccm3
747 simulation. *Ocean Modelling*, **In Press, Corrected Proof**, –, doi:DOI:10.1016/j.ocemod.
748 2011.02.011.
- 749 McWilliams, J., 2003: Diagnostic force balance and its limits. *Nonlinear processes in geo-*
750 *physical fluid dynamics*, Kluwer Academic Publishers.
- 751 Molemaker, M., J. McWilliams, and X. Capet, 2009: Balance and unbalanced routes to
752 dissipation in an equilibrated eady flow. *J. Fluid Mech.*, **submitted**.
- 753 Munk, W., 1950: On the wind-driven ocean circulation. *J. of Meteor.*, **7**, 79–93.
- 754 Nadiga, B. and D. Straub, 2010: Alternating zonal jets and energy fluxes in barotropic
755 wind-driven gyres. *Ocean Modelling*, **33**, 257–269.

- 756 Pedlosky, J., 1987a: *Geophysical Fluid Dynamics*. Springer-Verlag, 710 pp.
- 757 Pedlosky, J., 1987b: On Parsons' model of the ventilated thermocline. *Journal of Physical*
758 *Oceanography*, **17** (10), 1571–1582.
- 759 Pedlosky, J., 1996: *Ocean Circulation Theory*. Springer-Verlag, 453 pp.
- 760 Poulin, F., 2010: The linear stability of aperiodic baroclinic shear. *J. Phys. Oceanogr.*, **40**,
761 568–581.
- 762 Poulin, F. and G. Flierl, 2005: The influence of topography on the stability of jets. *J. Phys.*
763 *Oceanogr.*, **35**, 811–825.
- 764 Poulin, F., G. Flierl, and J. Pedlosky, 2010: The nonlinear dynamics of aperiodic baroclinic
765 shear. *J. Phys. Oceanogr.*, **40**, 1851–1865.
- 766 Rhines, P. and W. Holland, 1979: A theoretical discussion of eddy-driven mean flows. *Dyn.*
767 *Atmos. Ocean*, **3**, 289–325.
- 768 Schar, C. and R. Smith, 1993: Shallow-water flow past isolated topography. part i: Vorticity
769 production and wake formation. *J. Atmos. Sci.*, **50** (10), 1373–1400.
- 770 Schneider, K. and M. Farge, 2008: Final states of decaying 2d turbulence in bounded do-
771 mains: influence of the geometry. *Physica D*, **237**, 2228–2233.
- 772 Scott, R. and B. Arbic, 2007: Spectral energy fluxes in geostrophic turbulence: implications
773 for ocean energetics. *J. Phys. Oceanogr.*, **27**, 673–688.
- 774 Scott, R. and D. Straub, 1998: Small viscosity behavior of a homogeneous quasi-geostrophic,
775 ocean circulation model. *J. Mar. Res.*, **56**, 1225–1258.
- 776 Stommel, H., 1948: The westward intensification of wind-driven ocean currents. *Trans.*
777 *Amer. Geophys. Union*, **29**, 202–206.

- 778 Sverdrup, H., 1947: Wind-driven currents in a baroclinic ocean; with application to the
779 equatorial currents in the eastern pacific. *Proc. N.A.S.*
- 780 Thomas, L., A. Tandon, and A. Mahadevan, 2008: Submesoscale processes and dynam-
781 ics. *Ocean Modeling in an Eddying regime*, M. Hecht and H. Hasumi, Eds., American
782 Geophysical Union, Washington, DC, Geophysical Monograph Series, Vol. 177, 17–38.
- 783 Tran, C. and T. Shepherd, 2002: Constraints on the spectral distribution of energy and
784 energy dissipation in forced two-dimensional turbulence. *Physica D*, **165**, 199–212.
- 785 Vallis, G., 2006: *Atmospheric and Oceanic Fluid Dynamics*. Cambridge University Press,
786 Cambridge, U.K.
- 787 van Heijst, G. and H. Clercx, 2009: Studies on quasi-2d turbulence—the effect of boundaries.
788 *Fluid Dyn. Res.*, **41**, 064 002 (18pp).
- 789 van Heijst, G., H. Clercx, and D. Molenaar, 2006: The effects of solid boundaries on confined
790 two-dimensional turbulence. *J. Fluid Mech.*, **554**, 411–431.
- 791 Warn, T., 1986: Statistical mechanical equilibria of the shallow water equations. *Tellus A*,
792 **38A**, 1–11.
- 793 Zhai, X., H. Johnson, and D. Marshall, 2010: Significant sink of ocean-eddy energy near
794 western boundaries. *Nature Geosci.*, **3**, 608–612.

795 **List of Tables**

796 1 This is a sample table caption and table layout. Enter as many tables as
797 necessary at the end of your manuscript. Table from Lorenz (1963). Lengths
798 are all in are in kilometers.

38

TABLE 1. This is a sample table caption and table layout. Enter as many tables as necessary at the end of your manuscript. Table from Lorenz (1963). Lengths are all in are in kilometers.

ν (m ² /s)	δ_M	δ_I	δ_S	δ_{sm}	Re	grid	$N_x \times N_y$	ncpus	behaviour
1.6000×10^5	200	60	50	0.7	0.03	24	256×256	16	laminar
2.0000×10^4	100	89	25	1.6	0.7	24	256×256	16	laminar
2.5000×10^3	50	128	12.5	3.3	17	12	512×512	32	laminar
3.1250×10^2	25	166	6	5.5	293	5.9	1024×1024	64	eddies
3.9062×10^1	12.5	184	3	6.8	3190	2.9	2048×2048	128	turbulent

799 List of Figures

- 800 1 Plots of the zonal slice of the mean meridional velocity through the centre of
801 the domain for both the SW and QG simulations. As well, we plot vertical
802 lines that indicate the width of the Stommel and Munk boundary layers. 41
- 803 2 Plots of the time-series of kinetic energy, potential enstrophy as defined in
804 QG, available potential energy and potential enstrophy in SW for the five
805 different SW simulations that we previously defined. 42
- 806 3 Azimuthally integrated, time-averaged, one-dimensional energy spectra of ki-
807 netic energy, potential energy (multiplied by k^2), kinetic energy in the QG run,
808 zonal velocity and meridional velocity calculated using the wavelet transform
809 for the total solution between days 300 and 305. The two straight lines that
810 are superimposed have slopes $-5/3$ and -5 that match with the slope of the
811 KE in the intermediate and dissipative ranges. 43
- 812 4 The azimuthally integrated, time-averaged, one-dimensional energy spectra
813 of kinetic energy, potential energy (multiplied by k^2 and a constant), zonal
814 velocity and meridional velocity for the perturbation solution between days
815 300 and 305. The two straight lines that are superimposed have slopes -3 and
816 -5 that match with the slope of the KE in the intermediate and dissipative
817 ranges. 44
- 818 5 Subplots a) and b) show the vorticity fields of the QG and SW simulations at
819 day 300 well after turbulence has been generated in the north-west corner. The
820 white square depict a subdomain that is removed form the WBC and contains
821 a turbulent region. Subplots c) and d) show the corresponding spectra for the
822 QG and SW simulations, respectively. The different spectra that we present
823 are 1) Wavelet transform for the entire basin, 2) Wavelet transform for a region
824 in the south-western quadrant that is laminar and 3) Wavelet transform for
825 the subdomain in the north-west quadrant. 45

- 826 6 Spectral transfers and fluxes of the kinetic energy in the SW model due to
827 the wind forcing, lateral viscosity and bottom drag. This is obtained using
828 the Fourier approach by averaging the fluxes from days 400 to day 700. The
829 three dashed vertical lines indicate the wavenumber of the external Rossby
830 radius of deformation, the Charney scale and the Munk layer thickness from
831 left to right, respectively. 46
- 832 7 Spectral flux of the kinetic energy in the SW model due to the nonlinear
833 advection (T_k), the sum of the pressure and Coriolis terms (beta) and the
834 forcing and dissipation terms ($\tau+\nu+r$). This is obtained using the Fourier
835 approach by averaging the fluxes from days 400 to day 700. The three dashed
836 vertical lines indicate the wavenumber of the external Rossby radius of defor-
837 mation, the Charney scale and the Munk layer thickness from left to right,
838 respectively. 47
- 839 8 Spectral transfers (T_k) and fluxes (Π_k) due to nonlinear advection computed
840 for the SW and QG simulations obtained using the Fourier approach by av-
841 eraging the fluxes from days 400 to day 700. The three dashed vertical lines
842 indicate the wavenumber of the external Rossby radius of deformation, the
843 Charney scale and the Munk layer thickness from left to right, respectively.
844 In each subplot we have a zoom of the largest wavenumber that are resolved
845 to indicate that there is a direct energy transfer from the larger scales. 48

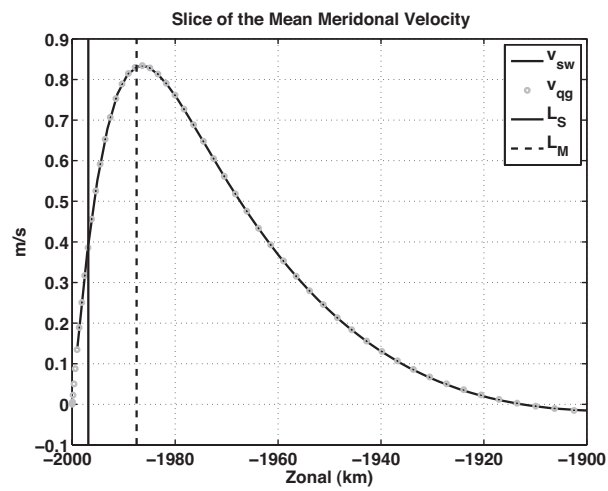


FIG. 1. Plots of the zonal slice of the mean meridional velocity through the centre of the domain for both the SW and QG simulations. As well, we plot vertical lines that indicate the width of the Stommel and Munk boundary layers.

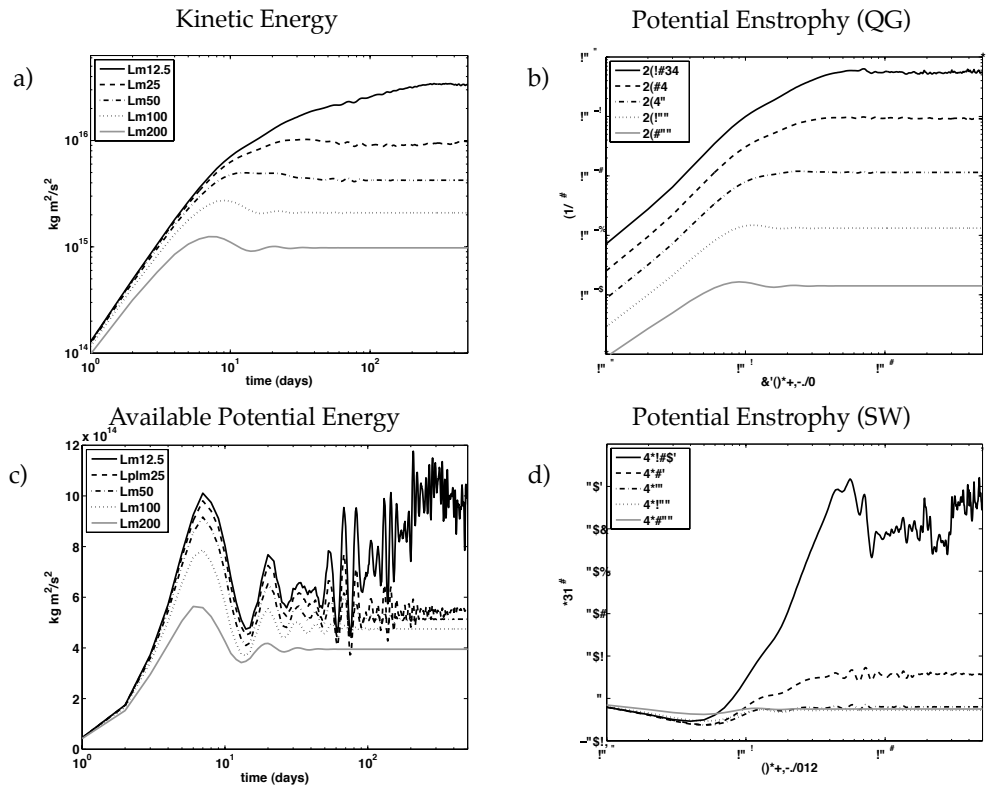


FIG. 2. Plots of the time-series of kinetic energy, potential enstrophy as defined in QG, available potential energy and potential enstrophy in SW for the five different SW simulations that we previously defined.

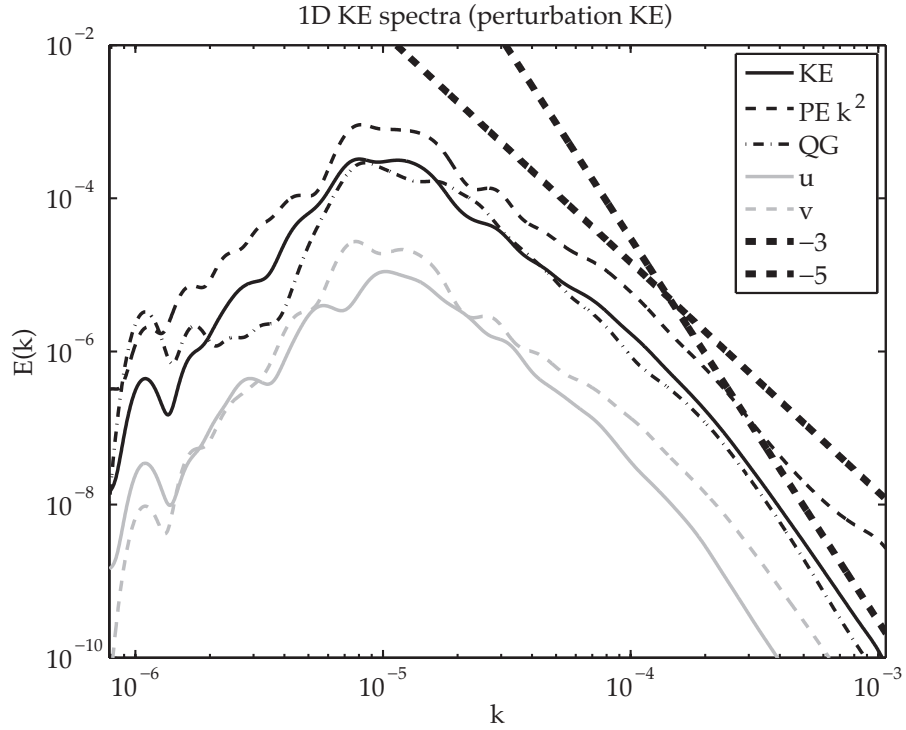


FIG. 3. Azimuthally integrated, time-averaged, one-dimensional energy spectra of kinetic energy, potential energy (multiplied by k^2), kinetic energy in the QG run, zonal velocity and meridional velocity calculated using the wavelet transform for the total solution between days 300 and 305. The two straight lines that are superimposed have slopes $-5/3$ and -5 that match with the slope of the KE in the intermediate and dissipative ranges.

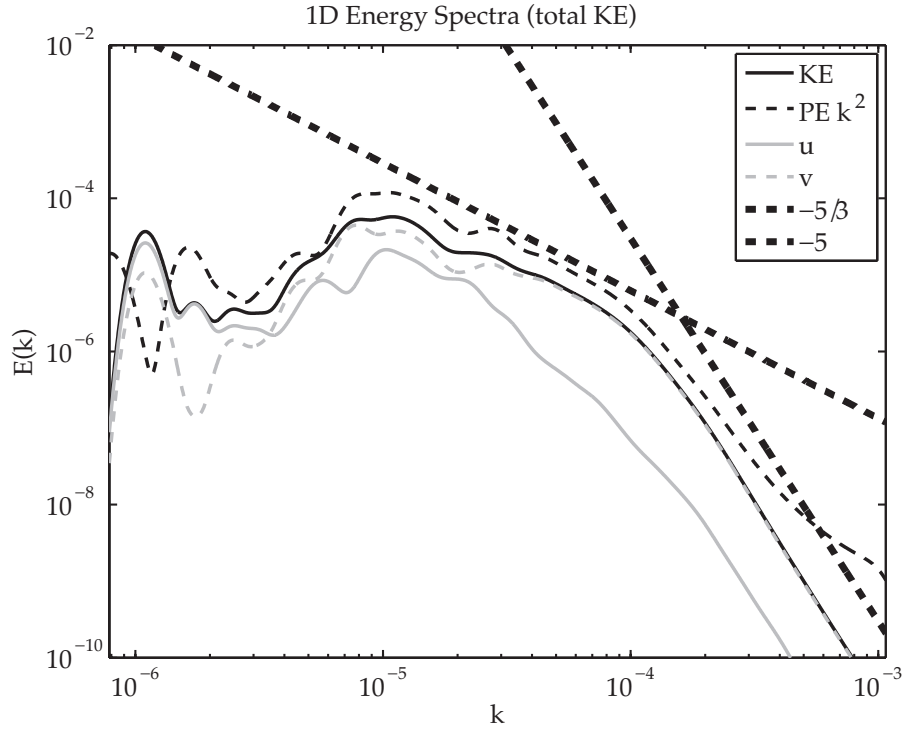


FIG. 4. The azimuthally integrated, time-averaged, one-dimensional energy spectra of kinetic energy, potential energy (multiplied by k^2 and a constant), zonal velocity and meridional velocity for the perturbation solution between days 300 and 305. The two straight lines that are superimposed have slopes -3 and -5 that match with the slope of the KE in the intermediate and dissipative ranges.

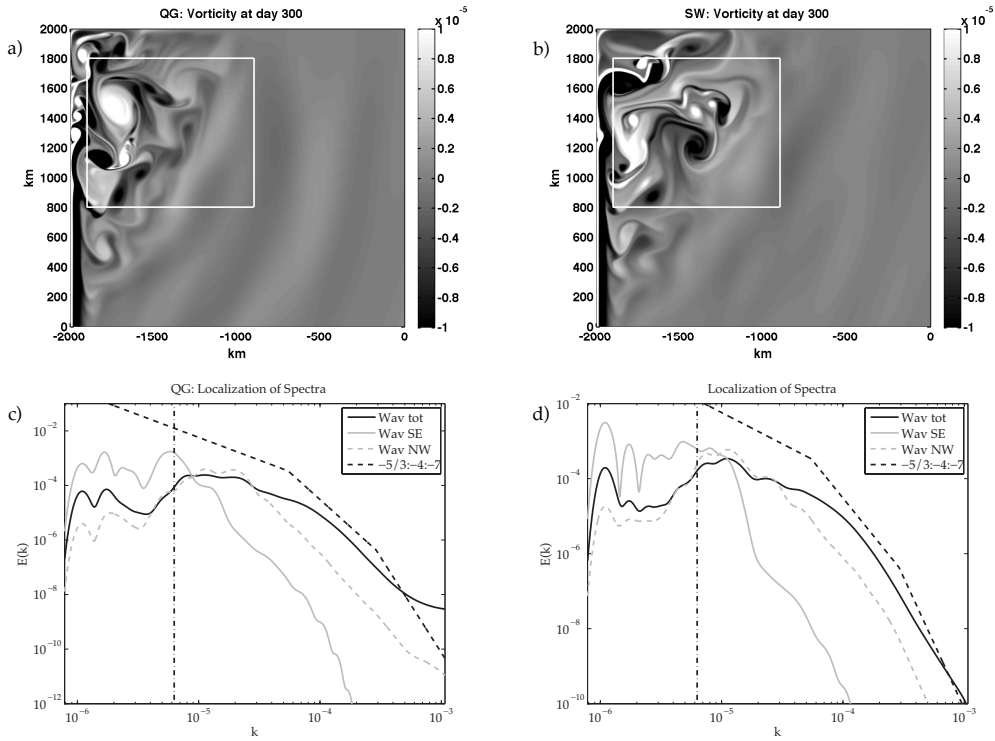


FIG. 5. Subplots a) and b) show the vorticity fields of the QG and SW simulations at day 300 well after turbulence has been generated in the north-west corner. The white square depict a subdomain that is removed form the WBC and contains a turbulent region. Subplots c) and d) show the corresponding spectra for the QG and SW simulations, respectively. The different spectra that we present are 1) Wavelet transform for the entire basin, 2) Wavelet transform for a region in the south-western quadrant that is laminar and 3) Wavelet transform for the subdomain in the north-west quadrant.

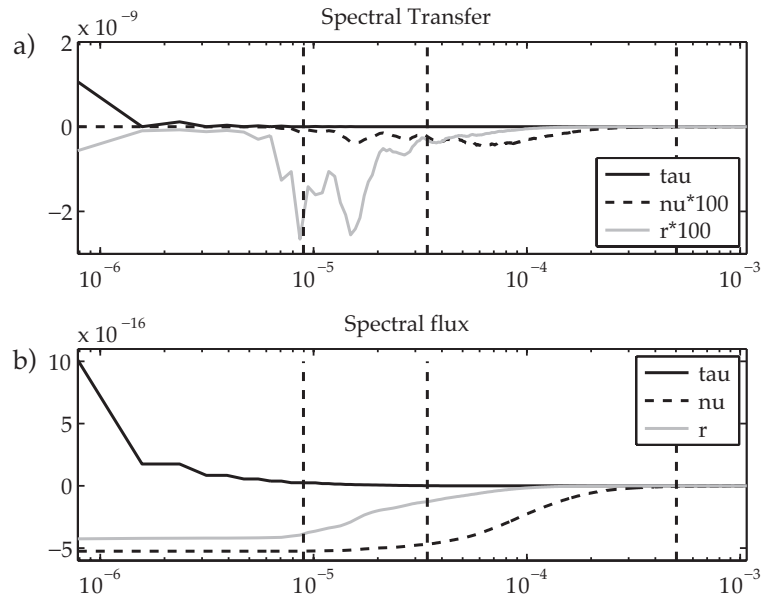


FIG. 6. Spectral transfers and fluxes of the kinetic energy in the SW model due to the wind forcing, lateral viscosity and bottom drag. This is obtained using the Fourier approach by averaging the fluxes from days 400 to day 700. The three dashed vertical lines indicate the wavenumber of the external Rossby radius of deformation, the Charney scale and the Munk layer thickness from left to right, respectively.

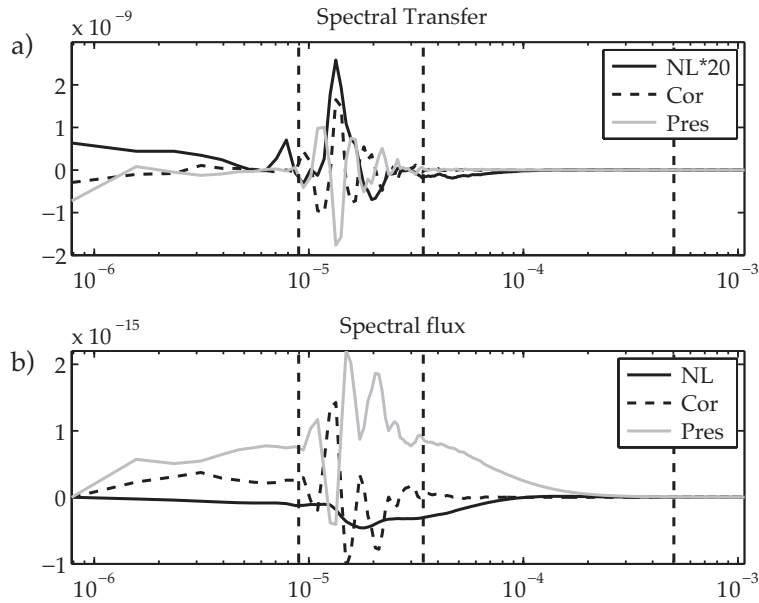


FIG. 7. Spectral flux of the kinetic energy in the SW model due to the nonlinear advection (T_k), the sum of the pressure and Coriolis terms (beta) and the forcing and dissipation terms ($\tau + \nu + r$). This is obtained using the Fourier approach by averaging the fluxes from days 400 to day 700. The three dashed vertical lines indicate the wavenumber of the external Rossby radius of deformation, the Charney scale and the Munk layer thickness from left to right, respectively.

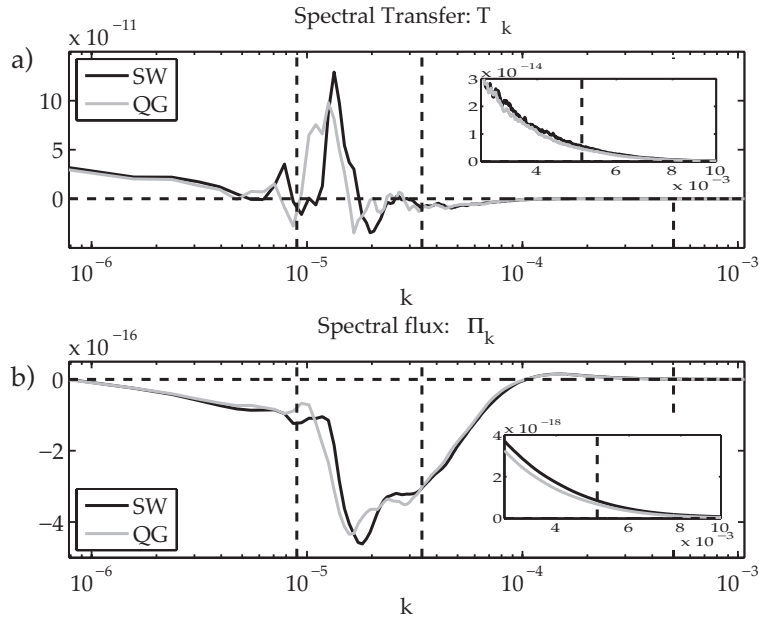


FIG. 8. Spectral transfers (T_k) and fluxes (Π_k) due to nonlinear advection computed for the SW and QG simulations obtained using the Fourier approach by averaging the fluxes from days 400 to day 700. The three dashed vertical lines indicate the wavenumber of the external Rossby radius of deformation, the Charney scale and the Munk layer thickness from left to right, respectively. In each subplot we have a zoom of the largest wavenumber that are resolved to indicate that there is a direct energy transfer from the larger scales.